$Al_xIn_{1-x}P$ LEDs with II-VI Cladding Layers for Efficient Red and Amber Emission

Final Scientific & Technical Report

DOE award number DE-SC0017063

Office of Science – U.S Department of Energy

MicroLink Devices, Inc.

Christopher L. Stender (P.I.)
MicroLink Devices, Inc.
6457 West Howard Street
Niles, IL 60714
Phone: 847-588-3001 x31
cstender@mldevices.com

Kirstin Alberi
National Renewable Energy Laboratory
15013 Denver West Parkway
Golden, CO 80401
Phone: 303-384-7647
Email: Kirstin.Alberi@nrel.gov

Period of Performance
February 21, 2017-November 20, 2017

Contents

Executive Summary 3

Summary of Project Activities (February – November 2017) 4

II-VI on III-V Template Development 4

AlInP and AlGaInP LED Development 8

Device Performance 11

Conclusion 13

Recommendations 14

Figure 1. The epitaxial layers grown to establish the growth of II-VI material in MBE at NREL……. 5
Figure 2. The PL map of the 6inch wafer serving as growth template for MBE of II-VI……... 5
Figure 3. (a) The structure grown by MLD to initiate the growth of II-VI films on MOVPE-grown phosphide-terminated films.(b) The PL map indicate the high level of wafer uniformity and fairly strong PL signal indicating good quality growth of the epilayers. (c)) The XRD scans of the film at the wafer center and close the edge of the wafer. An Indium content of 48.6% and 49.5% was resolved in the InGaP layer, at center and edge of the wafer, respectively…..... 6
Figure 4. Low temperature photoluminescence of a) ZnSe epilayers grown on GaAs and Ga0.5In0.5P surfaces directly after native oxide removal and b) Ga0.5In0.5P epilayers after ZnSe growth as a function of native oxide removal conditions……..... 7
Figure 5. The Effect of Temp. and Impurities on the growth of AlInP-on-MBLs as measured by XRD-RSM…… 8
Figure 6. The Effect of Temp. and doping on the growth of MBLs as measured by PL. The PL maps show the singal related to the MBL layer…….. 9
Figure 7. Low temperature PL from various AlInP layers. Annealing of the MBL increased the PL intensity from AlInP. The MBL with smaller lattice constant caused a blue-shift in the PL signal of the AlInP layer. AlInP grown at higher temperature has very weak PL signal and peak shift to higher energies (2.34eV)…… 9
Figure 8. An example of the data extracted from the state-of-the-art in-situ monitoring tool used for the growth of samples in this project: Growth of AlInP-on-MBL……. 10
Figure 9. TEM Analysis of AlInP-on-MBL structure……... 11
Figure 10. The LED structures which were grown in this project……... 11
Figure 11. LED double heterostructure used for this study……... 12
Figure 12. Performance of our champion AlxIn1-xP LED. a) LED IV curve (photograph in the inset), b) electroluminescence intensity as a function of drive current density, c) normalized photoluminescence spectra of the AlxIn1-xP and (AlxIn1-x)0.5In0.5P LED… 13

Executive Summary

The energy-saving promise of solid-state lighting (SSL) lies in the ultimate efficiency at which semiconductor devices can produce visible light. While SSL technology is already impacting the general and horticultural lighting markets, much head-room remains for improvement over current products. The phosphor-converted (pc) architecture that dominates among today's white light sources combines a direct-emitting blue light emitting diode (LED) with phosphors to down-convert that emission over a broad range of red and green wavelengths. This approach initially provided the simplest pathway toward commercial products, yet it inherently limits the energy-saving potential of SSL. At the same time, white pc-LEDs have already become a commodity on the world market and this architecture offers only modest room for performance improvements.

Next-generation hybrid and color-mixing (cm) SSL architectures reduce or altogether remove the limitations of pc-LEDs and offer additional pathways for enhanced performance. In a hybrid LED, the red phosphor is replaced with a red LED, while the cm-LED utilizes direct emitting red, green, blue and amber (RGBA) LEDs to cover the entire visible spectrum. Direct-emitting LEDs do not suffer from Stokes shift and infrared emission losses, enabling higher ultimate efficiencies. They also have design and functionality advantages. The narrow linewidths of direct-emitting LEDs produce saturated colors that yield a larger color gamut. The tighter radial distribution of light from direct-emitting LEDs rather than phosphor coatings also permits the use of simpler optical infrastructure that could reduce the cost of the luminaire. Finally, hybrid and cm architectures enable color control and tunability so that lighting can be designed for specific applications or to enhance the overall aesthetic experience of the user. These approaches are therefore well-suited to realize the full efficiency potential of SSL technologies while creating new market opportunities for innovative and transformational lighting products.

Practical realization of hybrid and cm LEDs will require substantial improvements in the power conversion efficiencies (PCE) and thermal stabilities of red and amber LEDs. Table 1 presents the status of LEDs operating at wavelength ranges across the visible spectrum. Both red and amber LEDs perform well below their theoretical maximum efficiencies of > 85%. Additionally, they suffer from poor thermal stability with hot/cold factors as low as 40%, further reducing efficiency at practical operating temperatures. The Department of Energy (DOE) highlights improvements in these areas as critical needs in the *Opportunity/Challenge 4: Red LED efficiency improvement* and *Opportunity/Challenge 5: Green/Amber LED efficiency improvement* sections of the Solid-State Lighting 2016 R&D Plan.[i] As discussed in detail in the next section, the efficiency and thermal stability challenges of red and amber LEDs result from fundamental material limitations of the $(Al_xGa_{1-x})_{0.51}In_{0.49}P$ alloys currently used in state-of-the-art devices. New materials and device designs are needed to overcome these limitations.

Table 1. Typical performance of best-available commercial LEDs.

Color	Peak Wavelength	Emitter Type	Spectral Halfwidth	Material	PCE [%] at 25°C	Hot/Cold Factor[1]	PCE [%] at 85°C
Blue	459 nm	Direct	20 nm	InGaN	66[(a)]	0.95[(b)]	63
Green	530 nm	Direct	30 nm	InGaN	24[(a)]	0.90[(b)]	22
Amber	595-605 nm	Phosphor-converted	80 nm	InGaN/ phosphor	23[(b)]	0.80[(b)]	18
Amber	585-595 nm	Direct	20 nm	AlGaInP	19[(b)]	0.40[(b)]	8
Red	615 nm	Direct	20 nm	AlGaInP	44[(a)]	0.55[(b)]	24
Deep Red	650-670 nm	Direct	20 nm	AlGaInP	49[(b)]	0.80[(b)]	39

Methodology: PCE values at 25°C and hot/cold factors are reported for best-known commercially-available devices in each color range; PCE value at 85°C is computed from the preceding columns. (a): SSL R&D Report 2016, Table 5.1; (b): estimated from Philips LUXEON Rebel performance (DS86, 2016).

*Hot/Cold Factor is defined as PCE(85°C) / PCE(25°C).

External losses due to electron leakage into the cladding layers of III-phosphide LEDs also constitute a major efficiency loss mechanism for red and amber LEDs under realistic operating conditions. Incumbent red and amber LED technologies utilize $(Al_xGa_{1-x})_{0.51}In_{0.49}P$ layers as both the active and cladding layers ($x_{active} < x_{clad}$), taking advantage of the bandgap increase with increasing Al concentrations. However, the relative band alignments in this alloy reveal that most of the band offset in such a heterostructure occurs at the valence band edge. Furthermore, the X conduction band minima decrease with Al concentration. As a result, the maximum electron confinements that can be achieved using this architecture (only 80 meV for amber LEDs) are inadequate for high drive currents and operating temperatures and contribute to the poor hot/cold factors in state-of-the-art phosphide LEDs.

Under this Small Business Technology Transfer project, MicroLink Devices and NREL made progress towards improving the efficiency of red and amber LEDs through the use of novel II-VI cladding layer and new AlInP material system to provide better confinement within the active layer. However, challenges persisted with surface preparation of III-V phosphides prior to MBE growth of the II-VI cladding layer resulting in deleterious recombination at the III-V/II-VI interface and poor emission properties. At the mid-term review the project received a slight refocus to include comparison between the lattice mismatched (LMM) AlInP and lattice matched (LM) AlGaInP material owing to the challenges remaining with II-VI growth on III-V phosphides. For our comparison non-optimized structures were used without quantum wells to improve efficiency. MicroLink Devices grew several variations of the AlGaInP LM and AlInP LMM structures targeting both amber (~580 nm) and red (~620 nm) ranges for our comparisons. Our team was able to show that optically pumped samples with LM and LMM structures demonstrate equivalent material properties which is a major achievement given LMM materials generally have significant threading dislocations that reduce luminescent intensity. We were unable to electrically pump our LM AlGaInP sample owing to a higher than anticipated doping in the active layer which resulted in no light emission. Our LMM AlInP sample grown at MicroLink and fabricated at NREL could be driven to high current densities up to 3 A/cm^2 without any heat sink before a reduction in the electroluminescence intensity from carrier loss due to inter-valley transfer, leakage and elevated temperatures was observed.

Summary of Project Activities (February – November 2017)

MicroLink Devices used an AIXTRON 2800 G4 MOVPE system to grow the required samples in this project. The growth was performed on a 6-inch substrates with 6-degree offcut to (111)-A. This system is used for the mass-production of high efficiency solar cells and a variety of other electronic device structures. It is capable of growing eight 6-inch wafers in a single run while recording the surface temperature, bow/curvature/stress, reflectance for each wafer individually *in-situ*. After the growth of each sample at MLD, a variety of ex-situ characterization is performed to assess the materials and micro-structural properties of the as-grown films in order to refine the growth process.

Some of *micro-structural* and *electrical* characterization methods include advanced XRD evaluations (Reciprocal Space Mapping RSM), full wafer Photoluminescence (PL) mapping, Hall measurements, Electro-Chemical Capacitance-Voltage (ECV), Epitaxial stress measurements, as well as Transmission and Reflectance measurements. MLD shares all growth and characterization details with NREL on a regular basis to be able to perform the R&D tasks efficiently.

<u>II-VI on III-V Template Development</u>

Growth of III-P templates by MOVPE for MBE growth of II-VI: The first area of development at NREL was to determine the best way to grow ZnSe on unprotected phosphide-based surfaces. The structure for the $Ga_{1-x}In_xP$ terminated MOVPE growth was chosen as a test bed for II-VI cladding layer over growth by NREL (

Figure **1**). PL maps of the structure shown in Figure 2 demonstrate a fairly uniform growth across the wafer. Further characterization using XRD showed excellent stoichiometric uniformity out to 68 mm radius from the center (Figure 3). Beyond 68 mm radius the GaInP epitaxial growth shows additional uptake of In resulting in the shoulder at ~200 arc seconds compressive. Several wafers with lattice matched GaInP film were grown and shipped to NREL to establish surface preparation and MBE growth conditions on phosphide terminated surfaces.

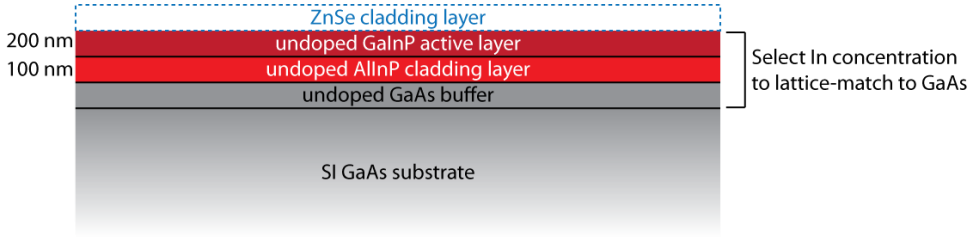

Figure 1. The epitaxial layers grown to establish the growth of II-VI material in MBE at NREL.

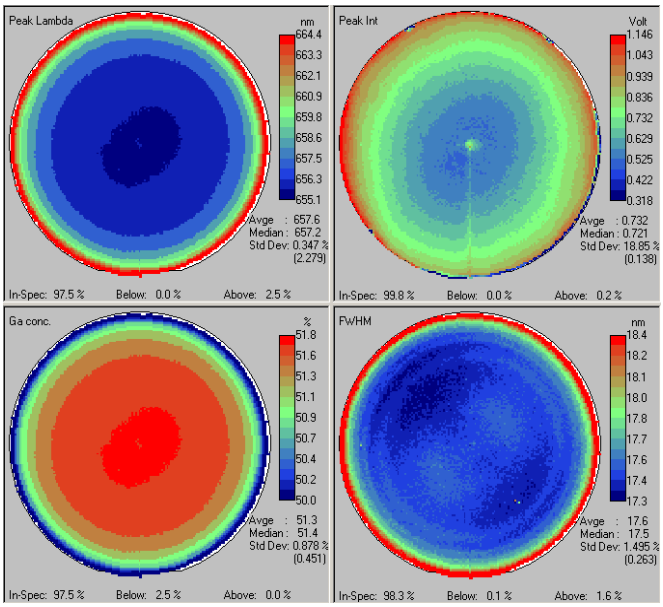

Figure 2. The PL map of the 6inch wafer serving as growth template for MBE of II-VI.

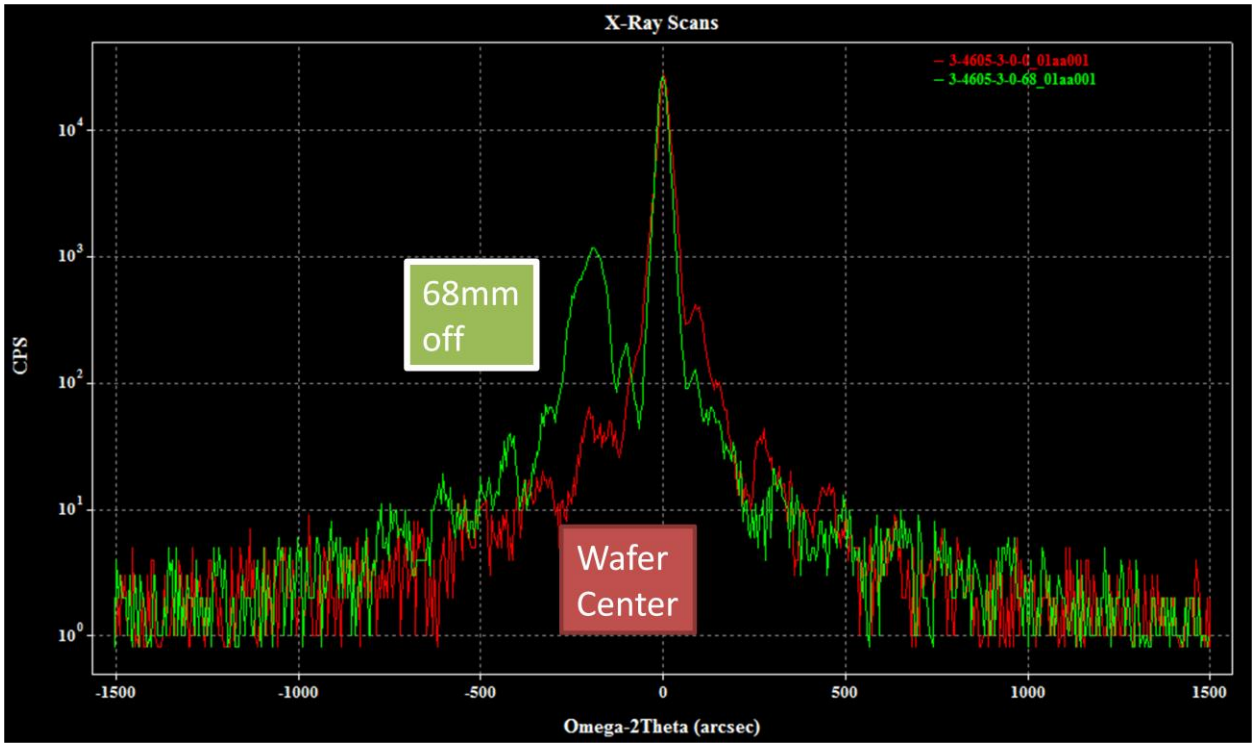

Figure 3. (a) The structure grown by MLD to initiate the growth of II-VI films on MOVPE-grown phosphide-terminated films. (b) The PL map indicate the high level of wafer uniformity and fairly strong PL signal indicating good quality growth of the epilayers. (c) The XRD scans of the film at the wafer center and close the edge of the wafer. An Indium content of 48.6% and 49.5% was resolved in the InGaP layer, at center and edge of the wafer, respectively.

Development of the p-type ZnSe-based cladding layer was carried out by molecular beam epitaxy (MBE) at NREL. Heteroepitaxial growth of II-VI semiconductors on III-V semiconductors is somewhat challenging because there must be a roughly equal mixture of II-V and III-VI bonds at the interface to maintain charge neutrality without the necessary formation of extra charged defects. NREL had previous experience growing high quality ZnSe epilayers on GaAs surfaces prepared in vacuum by applying a careful sequence of steps to initiate the interface formation. However, the collaborative nature of this project posed an additional complication to the ZnSe growth. Because the rest of the $Al_xIn_{1-x}P$ LED structure is grown first by MOCVD at MicroLink Devices, the top of the active layer is exposed to ambient conditions as it is shipped to NREL. The native oxide that forms on the $Al_xIn_{1-x}P$ surface must therefore be removed prior to ZnSe growth.

We first developed a combination of ex-situ wet chemical etching and in-situ hydrogen cleaning steps to remove the native oxide from GaAs surfaces. Using this procedure, we were able to replicate the ZnSe and interface quality that we were originally able to achieve on oxide-free GaAs surfaces. This procedure was then modified slightly to accommodate chemical etching of native oxides formed on lattice-matched $Ga_{0.5}In_{0.5}P$ surfaces as a test of whether it would work on phosphide-based surfaces. Subsequent epitaxial growth produced ZnSe epilayers of nearly the same quality to those grown on GaAs surfaces, as determined from x-ray diffraction and photoluminescence (PL) measurements (Figure 4a). However, we found the surface of $Ga_{0.5}In_{0.5}P$ to be less robust against oxide cleaning than GaAs. As a consequence, the poor quality of the ZnSe/$Ga_{0.5}In_{0.5}P$ interface reduced the radiative recombination efficiency of the underlying $Ga_{0.5}In_{0.5}P$ epilayer (see Figure 4b). This problem is aggravated in the case of $Al_xIn_{1-x}P$ surfaces due to the strong bonds that are formed between aluminum and oxygen. Alternative approaches of 1) initially capping the phosphide layer with a thin GaAs epilayer that was chemically removed immediately prior to loading into the MBE and 2) passivating any defects on the phosphide surface with either sulfur or selenium did not substantially improve the resulting optical emission. We believe that this problem is directly related to damage inflicted on the phosphide surface during oxide removal rather than the actual growth of the ZnSe epilayer. Therefore, we have reason to believe that such an approach would work if the epilayer structure were transferred from the $Al_xIn_{1-x}P$ growth chamber to the ZnSe growth chamber in vacuum.

The ZnSe epilayer also has to be doped p-type to operate as a cladding layer. The p-type doping efficiency of ZnSe has been known to be relatively low due to the deep position of acceptor states above the valence band and the propensity for compensating defects to spontaneously form. We have achieved room temperature free hole concentrations of around 10^{18} cm^{-3} by doping with nitrogen under constant exposure to UV photons during growth. While this should be sufficient for the purposes of the cladding layer, we have also experimented with grading tellurium into the ZnSe layer to reduce the depth of the acceptor states in the bandgap. This has led to two advantages. First, we have increased the free hole concentration to 10^{19} cm^{-3}, which will reduce series resistance in the cladding layer. Second, it has improved our ability to form Ohmic contacts using conventional metals such as indium. This approach now enables the use of ZnSe as a p-type cladding layer from a hole-injection perspective.

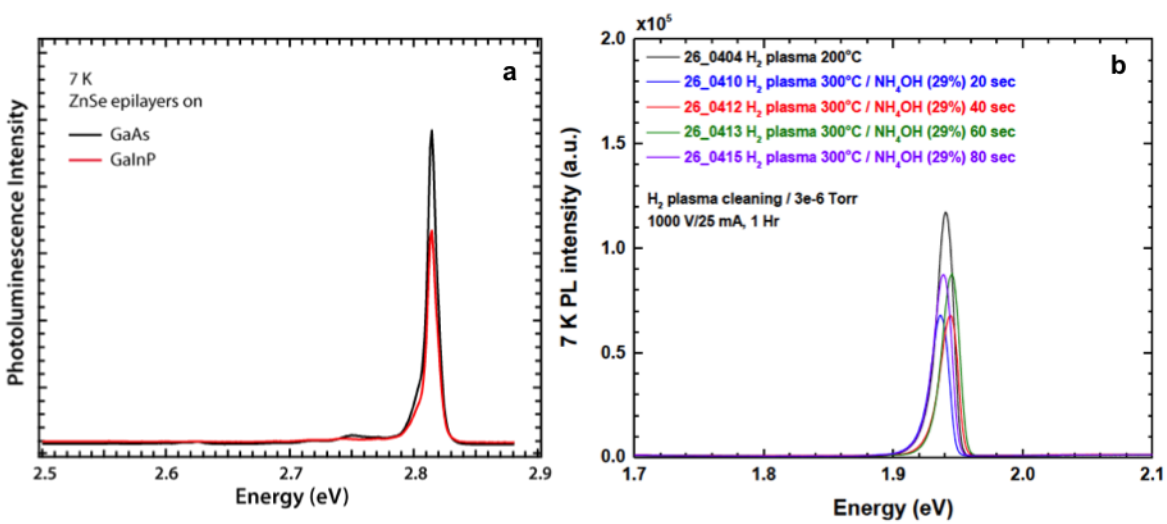

Figure 4. Low temperature photoluminescence of a) ZnSe epilayers grown on GaAs and Ga0.5In0.5P surfaces directly after native oxide removal and b) Ga0.5In0.5P epilayers after ZnSe growth as a function of native oxide removal conditions.

AlInP and AlGaInP LED Development

During the second half of the development effort we refocused the project to concentrate on LMM $Al_xIn_{1-x}P$ and LM $(Al_xGa_{1-x})_{0.5}In_{0.5}P$ LED structures. The intent was to compare an industry standard LM $(Al_xGa_{1-x})_{0.5}In_{0.5}P$ material system performance with our new material system LMM ($Al_xIn_{1-x}P$) in an effort to determine the benefits of the increased electron confinement.

Metamorphic buffer layers (MBLs) are commonly used in the growth of highly mismatched epitaxial layers. They are an enabling technology for multijunction solar cells when there is a need to grow e.g. InGaAs (1eV, 30%In) on GaAs, corresponding to a lattice constant misfit of 1.8%.

In this work, we had to realize $Al_xIn_{1-x}P$ (around 64% In) epitaxial layers on GaAs substrates. That corresponds to a roughly 0.9%-1% lattice misfit between the parent GaAs substrate and the epitaxial layers (active layer and claddings). We designed a specific MBL to be used in this project and studied the effect of annealing and dopants on the MBL growth. Figure 5 shows the XRD reciprocal space maps from three different MBLs. All of the MBLs presented in Figure 5 have an $Al_xIn_{1-x}P$ active layer grown on top. The RSM from an undoped MLB is shown on the left in Figure 5. Since the MBL is undoped, there is a crystallographic tilt of -600" toward the substrate miscut. The subsequent layer adapts this tilt value as shown in the RSM image in Figure 5. Contrast doping the MBL with Si results in the crystallographic tilt of around 1400". Furthermore, growing the $Al_xIn_{1-x}P$ at lower temperatures (50°C less) results in a tilt of around 2000" for all the layers including the MBL. That means annealing the MBL results in reduced titling of MBL even after it is grown. Clearly the MBL microstructure may affect the LED epitaxial growth quality. Shown in Figure 6 are the PL maps of the wafers presented in Figure 5. The wafer with the MBL design that was doped with Si and had higher temperature growth of the subsequent AlInP layer exhibits much stronger PL signal.

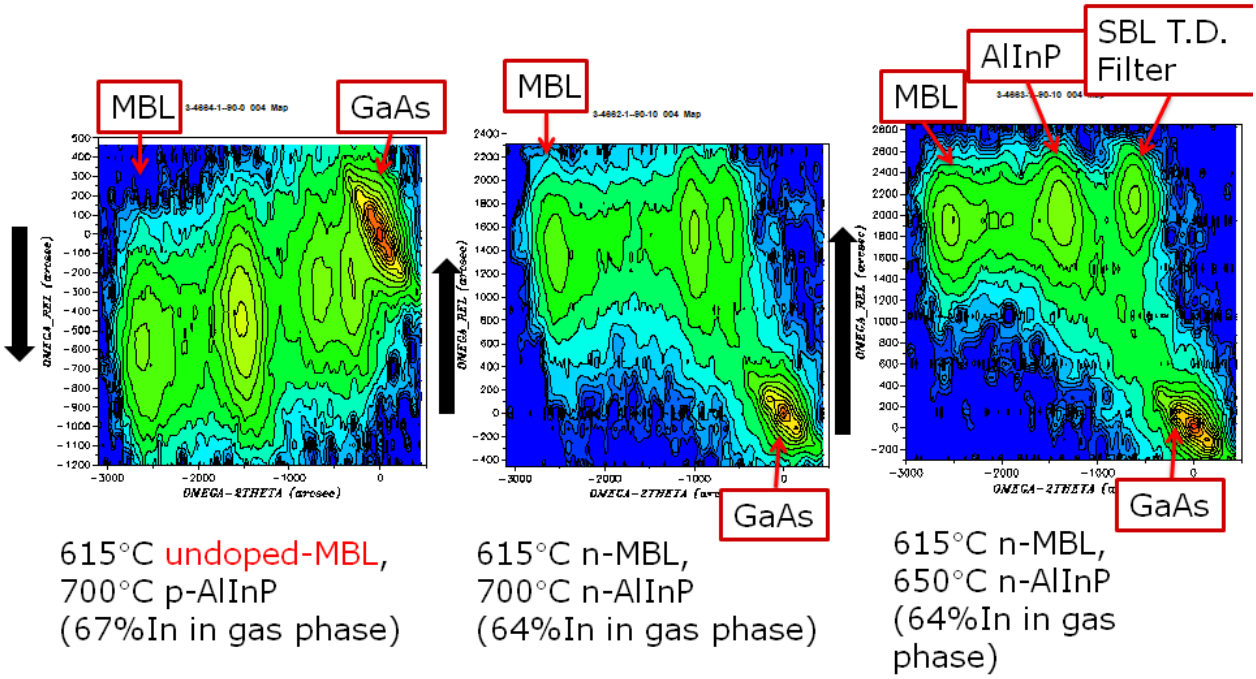

Figure 5. The effect of temp. and impurities on the growth of AlInP-on-MBLs as measured by XRD-RSM.

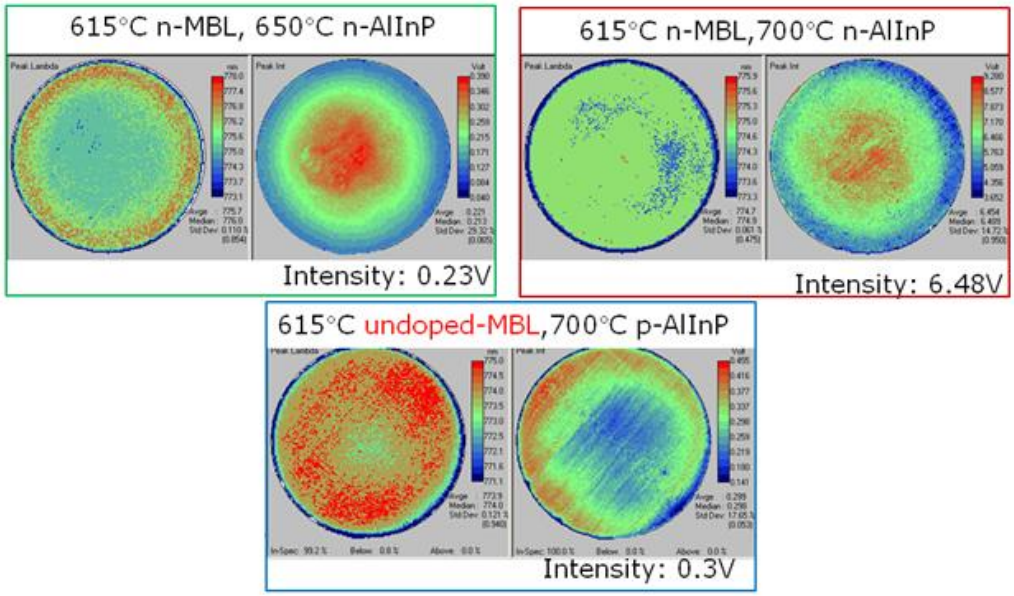

Figure 6. The effect of temp. and doping on the growth of MBLs as measured by PL. The PL maps show the signal related to the MBL layer.

Figure 7 summarizes the $Al_xIn_{1-x}P$-on-MBL optimization efforts. Low temperature PL evaluations indicated a strong PL from the samples grown at 650°C at around 2.1 eV. Annealing the MBL at 700°C for 7 min resulted in further increase of the PL intensity. Moreover, reducing the in-plane lattice constant of the MBL results in the blue-shift of PL spectra obtained from the $Al_xIn_{1-x}P$ layer. That can be due to the induced compressive stress into epi-layer and also more In rejection from the surface (lattice-latching effect). The $Al_xIn_{1-x}P$ layer grown at higher temperatures (700°C) shows a weaker PL peak at higher energies (2.34 eV). That can be due to the reduced ordering and In-content in the crystal structure. Growth temperatures around 700°C or higher are known to induce disordering and an increased In desorption rate causing the film composition become more Al-rich.

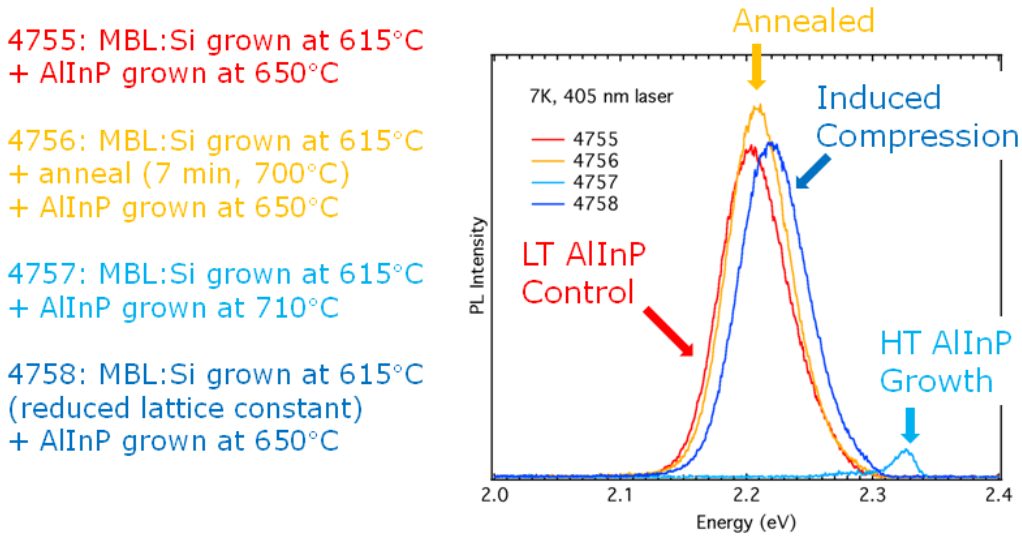

Figure 7. Low temperature PL from various AlInP layers. Annealing of the MBL increased the PL intensity from AlInP. The MBL with smaller lattice constant caused a blue-shift in the PL signal of the AlInP layer. AlInP grown at higher temperature has very weak PL signal and peak shift to higher energies (2.34 eV).

Figure 8 shows the in-situ data collected during the growth of an optimized $Al_xIn_{1-x}P$-on-MB-on-GaAs. The MOCVD system is capable is showing the true surface temperature during the growth run. This is crucial parameter needed to evaluate the repeatability of the experiments. The surface temperature is very stable for the growth of both the MBL and the $Al_xIn_{1-x}P$ as can been seen in Figure 8. The in-situ reflectance is also stable for the growth of both the MBL layer and the $Al_xIn_{1-x}P$ layer suggesting a smooth growth front with layer-by-layer growth mode. The curvature of the wafer is observed to drop during the growth of the MBL. This drop is indicative of an induced compressive stress from an epilayer with larger lattice constant: AlGaInAs(0% -- 20%In). After the growth of MBL, there is thin strain balancing layer (SBL) and dislocation filter as also indicated in Figure 8. The $Al_xIn_{1-x}P$ growth follows the growth of SBL and dislocation filter. Accordingly, the slope of the curvature signal reversed, indicating that the $Al_xIn_{1-x}P$ is grown under tensile stress. The SBL and dislocation filter were inserted to realize smoother surfaces with low cross-hatching, allowing for more homogeneous compositions. In this case, it is projected that the growth under compression has more drawbacks compared to the growth under tension. The red and blue curvature graphs show different levels of tensile stress in the $Al_xIn_{1-x}P$ layer caused by varying the MBL lattice constant. The blue curve represents the MBL sample with smaller lattice constant, inducing less tensile stress in the $Al_xIn_{1-x}P$. The PL from each sample was shown in Figure 7.

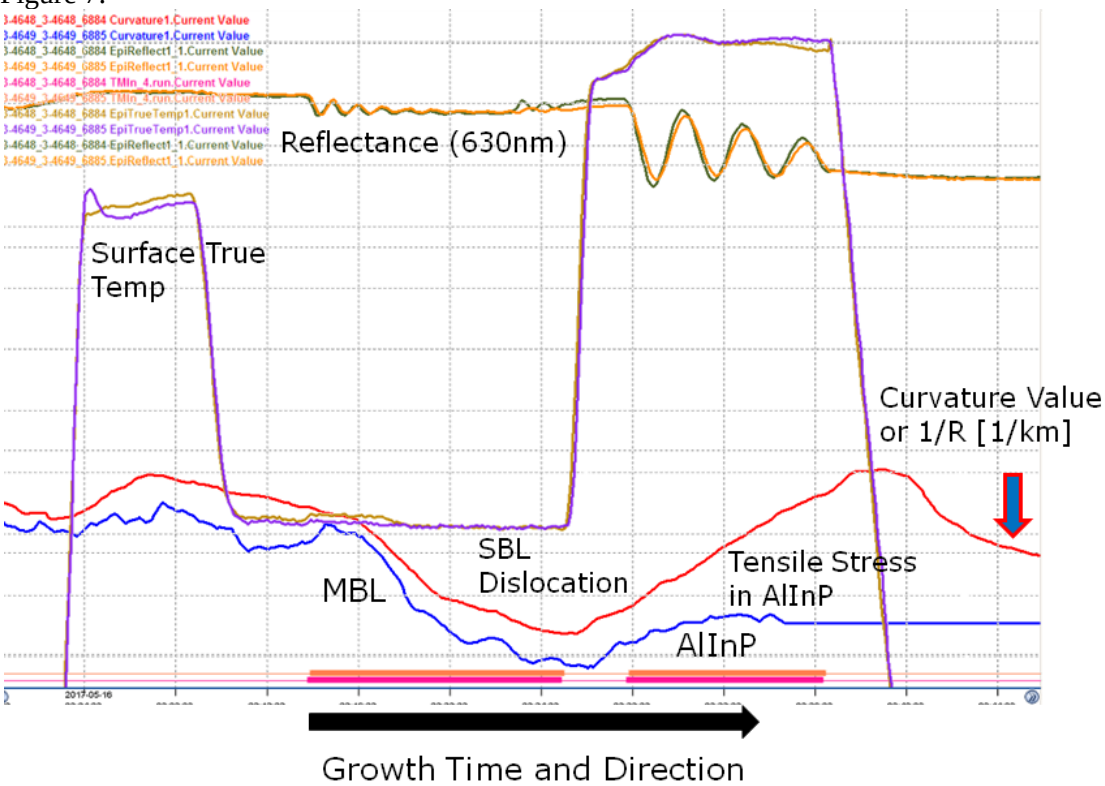

Figure 8. An example of the data extracted from the state-of-the-art in-situ monitoring tool used for the growth of samples in this project: Growth of AlInP-on-MBL.

TEM evaluations were performed to assess the behaviors of the dislocations within the epitaxial layer (Figure 9). The dislocations are mainly created during the first few hundred nanometers of the MBL and then their density reduces significantly. This is expected from the MBL design. The stress in the MBL is highest at the beginning of the layer and decreases non-linearly through the MBL. The stress is relaxed through the formation of misfit dislocations. As it is clearly visible in Figure 9, almost all dislocations are blocked at the interface between the MBL and dislocation filter layer. This shows the successful implementation of a dislocation filter in the MBL design for industrial wafer scales. Accordingly, the subsequent $Al_xIn_{1-x}P$ active/cladding layer is dislocation-free in this cross-sectional TEM image. The Al-

$_xIn_{1-x}P$ exhibits a high degree of compositional homogeneity. The TEM electron diffraction patterns indicate that the $Al_xIn_{1-x}P$ films grown at 650°C exhibit a high degree of ordered atomic structure (Figure 9-inset). This is in line with various reports in the literature for the $Al_xIn_{1-x}P$ alloys grown at around 650°C.

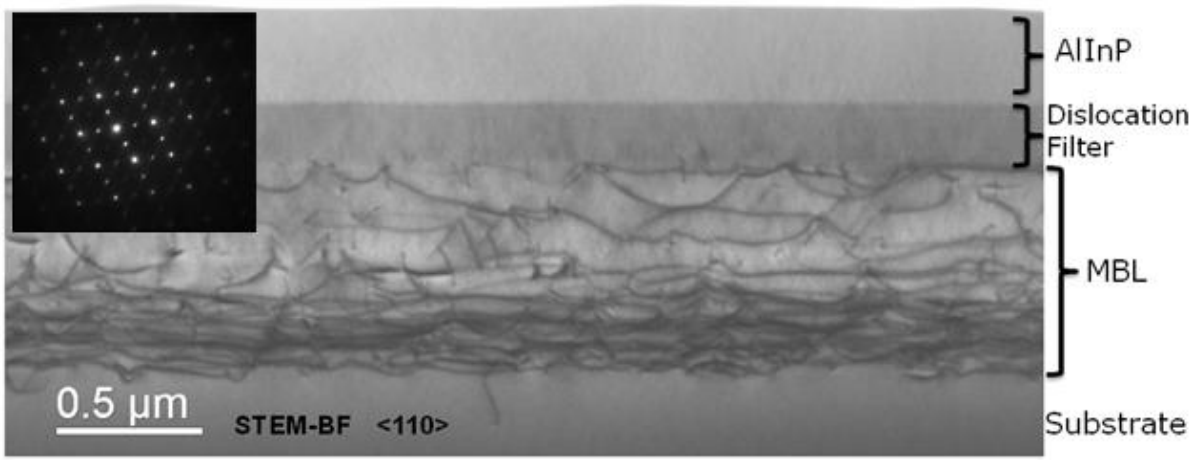

Figure 9. TEM Analysis of AlInP-on-MBL structure.

Shown in Figure 10 are the layer designs for three different LED structures that were grown based on the studies presented above. An AlInP-AlInGaP active layer lattice matched to GaAs was grown as a control device. An MBL-based LED with ternary AlInP active layer was grown as an alternative route to realize amber/green LEDs. This design offers the potential to realize efficient amber/green LEDs based on the advanced MBL technology to access new wavelengths. The third structure incorporates a hybrid MOVPE-MBE growth approach in which III-V is grown by MOVPE at MLD and the top II-VI later by NREL using MBE. All the structures were grown and shipped to NREL for device processing and analysis.

Figure 10. The LED structures which were grown in this project.

Device Performance

Several devices with a "standard LED design" and an "AlInP LED design" were fabricated to test performance. Since the ZnSe cladding layers were not yet ready for demonstration in a device, we constructed the devices entirely out of $Al_xIn_{1-x}P$. A simplified LED layer design consisting of a double heterostructure (Figure 11) was implemented in order to probe the optical quality of these epilayers grown on relaxed metamorphic buffer layers. This approach removes some of the additional complexity of optimally growing multiple quantum wells in the active region, which are typically used in conventional lattice-matched $(Al_xGa_{1-x})_{0.5}In_{0.5}P$ red and amber LEDs to improve the overall efficiency. Because the

lattice constant of the device layers is set by the underlying metamorphic buffer layers, electron confinement was incorporated through variation of spontaneous atomic ordering of Al and In atoms in the $Al_xIn_{1-x}P$ active and cladding layers. Ordering is known to reduce the bandgap of the alloy by lowering the conduction band edge by as much as 200 meV in $Al_xIn_{1-x}P$.[ii] Thus, cladding layers grown with disordered atomic arrangements provide electron confinement for light-emitting active layers grown with ordered atomic arrangements. We estimate that our $Al_xIn_{1-x}P$ LEDs have conduction band offsets of approximately 150 meV based on photoluminescence measurements of the cladding and active layers.

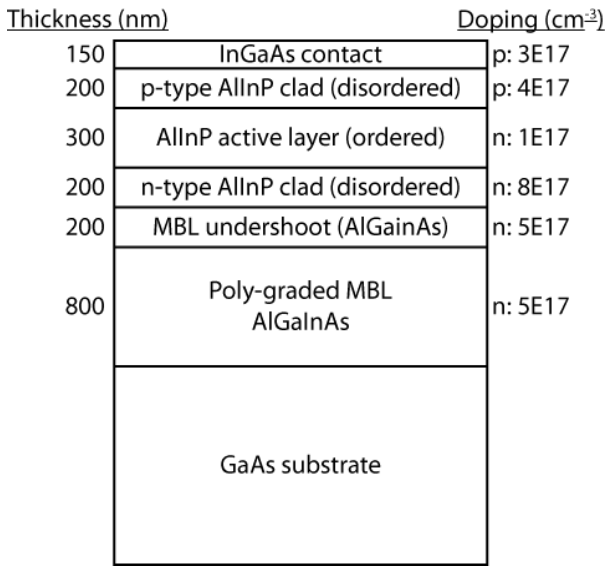

Figure 11. LED double heterostructure used for this study.

The current-voltage (IV) curve of our best AlInP active layer device is shown in Fig. 12a, and its corresponding electroluminescence is displayed in Figure 12b. The LED can be driven at high current densities up to 3 A/cm^2 before there is a reduction in the electroluminescence intensity due to carrier loss from inter-valley transfer, leakage and elevated temperatures. While the emission wavelength of this device (620 nm) was slightly longer than our target (~590 nm), these results indicate that the LED is well behaved even when it is grown at large lattice constant mismatch to the GaAs substrate.

We also tested a lattice-matched $(Al_xGa_{1-x})_{0.5}In_{0.5}P$ LED with the same simplified double heterostructure design. The extrinsic doping profiles of this device were not yet optimized, and the device exhibited non-ideal IV characteristics. We have therefore made a comparison between the devices by optically rather than electrically pumping them. The room temperature photoluminescence (PL) spectra of the $Al_xIn_{1-x}P$ and $(Al_xGa_{1-x})_{0.5}In_{0.5}P$ LEDs are shown in Figure 12c, and the PL intensities as a function of laser pump power density are displayed in Figure 12d. The PL intensities from the active layers of both devices exhibit similar trends as a function of laser power density, indicating that there are no major additional loss factors in the $Al_xIn_{1-x}P$ material. Thus, the $Al_xIn_{1-x}P$ material grown on a lattice-mismatched GaAs substrate is of comparable quality to the lattice-matched $(Al_xGa_{1-x})_{0.5}In_{0.5}P$ material, suggesting that the lattice-mismatch between the $Al_xIn_{1-x}P$ device layers and the GaAs substrate does not impact the device performance.

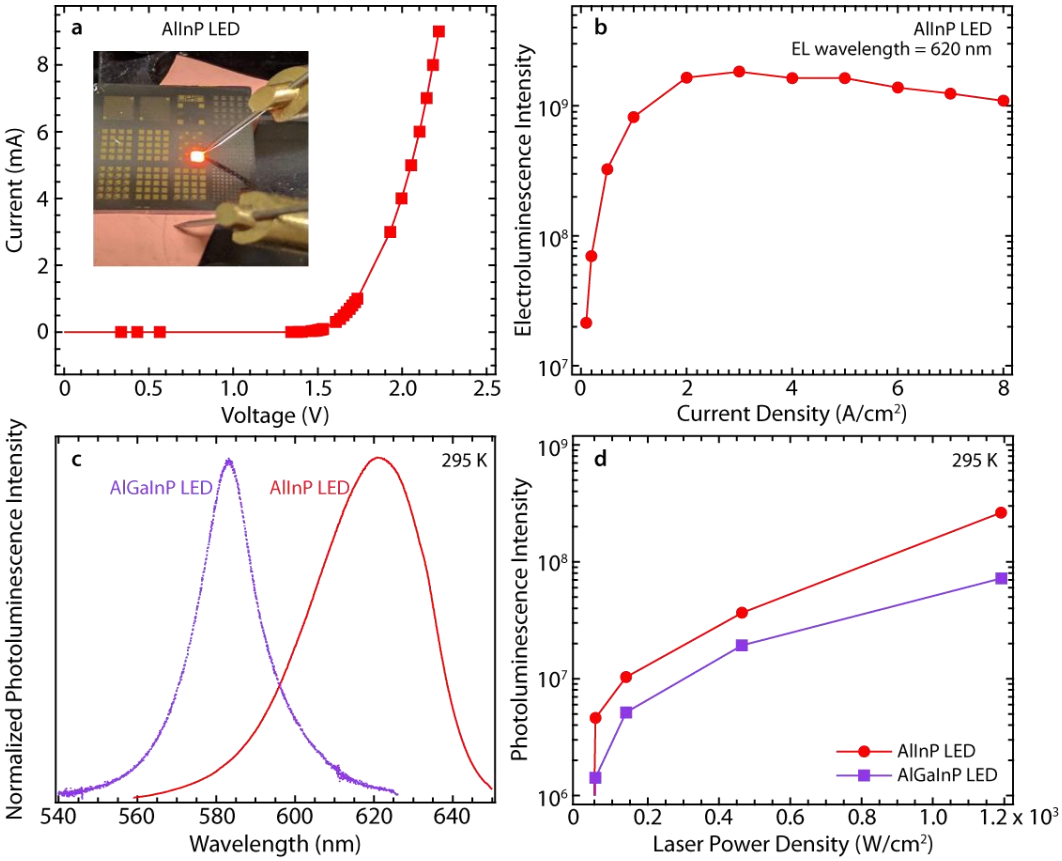

Figure 12. Performance of our champion AlxIn1-xP LED. a) LED IV curve (photograph in the inset), b) electroluminescence intensity as a function of drive current density, c) normalized photoluminescence spectra of the AlxIn1-xP and (AlxIn1-x)0.5In0.5P LED

Some additional work is needed to optimize the composition and growth of the metamorphic buffer layer and $Al_xIn_{1-x}P$ LED layers for emission at 590 nm as well as improve the extrinsic doping profile of the lattice-matched $(Al_xGa_{1-x})_{0.5}In_{0.5}P$ LED structure. Both tasks are not expected to run into any major barriers, especially since shortening the emission wavelength of the $Al_xIn_{1-x}P$ LED also reduces lattice mismatch between the device and substrate. Once they are completed, we can perform an in-depth comparison between equal LED structures to evaluate the effectiveness of $Al_xIn_{1-x}P$ to suppress carrier losses.

Conclusion

MicroLink Devices, in collaboration with NREL, started initial development of novel II-VI cladding layers on III-P and LMM AlInP LEDs for amber and red emissions to improve electron confinement compared to the standard AlGaInP material. Significant progress was made on regrowth of II-VI on III-P materials. However, surface oxide removal from phosphide surfaces formed during exposure to ambient conditions for prolonged periods of time resulted in poor quality interfacial regions that proved challenging to reconcile in the time frame allotted to this program. However, we do not believe this is a fundamental materials limitation but a logistical engineering challenge. NREL achieved a high p-type doping level (10^{19} cm^{-3}) in the II-VI cladding layer through the use of nitrogen and constant UV light exposure.

During the mid-term review the scope of work was redirected to include a comparison between the industry standard LM AlGaInP and LMM AlInP material systems owing to the challenges with II-VI

regrowth on III-P. A problem occurred during the MOPVE growth of the LM AlGaInP sample causing higher than intended doping of the active layer resulting in electrically inactive devices. Subsequent growths have rectified the problem but processing and analysis was not possible prior to this report. We will include the findings in our Phase II proposal for continuation of this work. NREL was able to optically pump both "standard LED design" and "AlInP LED design" to determine a general material quality comparison. Both samples demonstrated comparable epitaxial quality indicating a very low dislocation density in the LMM AlInP material. Dislocation density was seen as a major challenge for achieving high quality LMM AlInP LED materials. A LED from the AlInP structure was fully fabricated on substrate and demonstrated well behaved IV characteristics and 3 A/cm^2 drive current before a reduction in electroluminescence was observed.

Recommendations

During the interim period between this report and the Phase II proposal we will finish fabrication and analysis of "standard LED design" (580 and 620 nm) and "AlInP LED design" (580 and 620 nm) structures. Phase II will focus on improving the efficiency of the AlInP LED structure design to include QW, back reflectors and other state of the art designs features to push the limits of the LMM AlInP material. Additionally, we will explore substrate removal via epitaxial lift-off (ELO), a core competence and technology at MicroLink Devices. ELO has two main potential benefits 1) substrate reuse as a cost saving model and 2) facile integration of back reflector and heat sinking material.

---

[i] Department of Energy R&D Plan, 2016
[ii] T.M. Christian, *et al.*, *J. Appl. Phys*., **114**, 074505 (2013).